Catalytic Vapour Phase Hydrodehalogenation of 1,8-dichlorooctane over Pd@MIL-101(Cr)-NH_2: A Step Forward in MOF-Based Technologies

Raúl M. Guerrero [a,b,c], Ignacio D. Lemir [a,b], Carlos Fernández-Ruiz [a,b], Sergio Carrasco [a], Patricia Horcajada [a], David P. Serrano [b,d], Yolanda Pérez [a,e*], Patricia Pizarro [b,d*].

[a] *Advanced Porous Materials Unit, IMDEA Energy Institute, Avda. Ramón de la Sagra, 3, Móstoles, 28935 Madrid, Spain*
[b] *Thermochemical Processes Unit, IMDEA Energy Institute, Avda. Ramón de la Sagra, 3, Móstoles, 28935 Madrid, Spain*
[c] *Escuela Internacional de Doctorado, Rey Juan Carlos University, C/ Tulipán, s/n, Móstoles, 28933 Madrid, Spain*
[d] *Chemical and Environmental Engineering Group, Rey Juan Carlos University, C/ Tulipán, s/n, Móstoles, 28933 Madrid, Spain*
[e] *COMET-NANO Group, ESCET, Universidad Rey Juan Carlos, C/ Tulipán, s/n, Móstoles, 28933, Madrid, Spain*

[*]**Corresponding Author E-mail:** **yolanda.cortes@urjc.es** (Y. Pérez);

patricia.pizarro@imdea.org (P. Pizarro).

1. Materials and methods

1.1 Synthesis of catalysts

Materials

All chemicals used in this study were purchased from commercial suppliers and utilized without additional purification treatments: Chromium (III) nitrate nonahydrate ($Cr(NO_3)_3 \cdot 9H_2O$, Acros Organics, 99%), 2-aminoterephthalic acid (2-ATA, Acros Organics, 99%), potassium fluoride (KF, Acros Organics, 99%), palladium (II) chloride ($PdCl_2$, Merck, 99%), sodium borohydride ($NaBH_4$, Sigma Aldrich, 98%), absolute ethanol (Molecular Biology Grade, Fisher), acetone (HPLC Grade, Chem-lab) and tetrahydrofuran (THF, Chem-Lab, 99.9%). Additionally, a commercial catalyst, Pd(5 wt.%)/Al_2O_3, was acquired from Sigma-Aldrich for comparison purposes. To prepare the model feed representing the chlorinated contaminant, 1,8-dichloroctane (Sigma Aldrich, 98%) and n-decane (VWR, 99%) was purchased.

1.2 Catalyst characterization

Fourier-transform infrared spectroscopy (FTIR) spectra were collected using a Nicolet 6700 spectrometer (Thermo Scientific, USA) in attenuated total reflectance (ATR) mode with a diamond accessory. FTIR spectra were acquired over 32 scans at a resolution of 4 cm^{-1} across the wavenumber range of 4000-400 cm^{-1}. Powder X-ray diffraction (PXRD) patterns were obtained using a PANalytical® Empyrean powder diffractometer (PANalytical, Lelyweg, The Netherlands) equipped with Cu Kα radiation (λ = 1.5406 Å) in reflection mode. The 2Θ scan range was set to 3-50º for MOFs and 3-90º for composites, with a step size of 0.013º and a scanning speed of $0.1^{o} \cdot s^{-1}$. Variable-temperature PXRD (VTPXRD) measurements were performed on a D8 ADVANCE Bruker AXS θ-2θ diffractometer, utilizing Cu Kα radiation (λ = 1.54060 Å). The

instrument was equipped with an Anton Paar XRK 900 high-temperature chamber and a LYNXEYE XE detector, operating under 40 kV and 40 mA conditions.

Thermogravimetric analyses (TGA) were conducted using an SDT Q-600 thermobalance (TA Instruments, New Castle, DE, USA). Samples were heated from room temperature to 800 ºC under oxidative conditions (air flow rate: 100 $mL \cdot min^{-1}$) at a heating rate of 5 $ºC \cdot min^{-1}$. Nitrogen adsorption-desorption isotherms were measured at 77 K using a Micromeritics Tristar II PLUS analyzer. Samples (approximately 50-100 mg) were previously degassed at 150 ºC for 16 h under vacuum. The specific surface area was calculated using the Brunauer-Emmett-Teller (BET) equation within a relative pressure range of P/P_o = 0.01-0.30. Micropore size distribution was determined using the Horvath-Kawazoe (HK) method (spherical model) and mesopore size distribution was determined using Barrett-Joyner-Halenda (BJH) method, while pore volume and area were estimated using the t-plot method in the relative pressure range of P/P_o = 0.01-0.80.

Inductively coupled plasma optical emission spectroscopy (ICP-OES) was performed using a Perkin Elmer Optima 7300 DV after sample digestion in piranha solution. Routine transmission electron microscopy (TEM) images were acquired using a JEOL JEM 1400 FLASH microscope operating at 200 kV, using copper grids coated with amorphous carbon. Elemental analysis was performed using energy-dispersive X-ray spectroscopy (EDS) with a secondary detector, and surface composition was analyzed using X-ray photoelectron spectroscopy (XPS) performed on a SPECS PHOIBOS150 MCD system with a monochromatic Al Kα source; binding energies were referenced to the C 1s peak at 284.5 eV. Field emission scanning electron microscopy (FE-SEM) images were captured with a JEOL JSM 7900F microscope at an accelerating voltage of 10 kV.

1.3 Products analysis

Total mass balances were quantified by the weight of the different fractions collected from the reaction. The coke content accumulated on the catalyst was estimated through TGA by weight difference of the catalyst before and after combustion in air atmosphere. In all HDH assays, the total mass balance was close to 100 wt.%. Furthermore, the carbon balance was assessed through elemental analysis of C, H, N, and S in the liquid phases (feed and treated oils) and the catalyst. The gas composition was analyzed using a micro-GC analyzer (Agilent 490 Micro-gas chromatograph) equipped with a molecular sieve (Molsieve 5Å) and PPQ columns, and a thermal conductivity detector (TCD). All reactions closed the C mass balance above 96%.

Treated oils were analyzed by gas chromatography coupled with mass spectrometry (GC-MS) using an Agilent 7693A GC-5977B GC/MSD equipped with a HP5-MS UI column (30 m x 0.25 mm x 0.25 μm). The oils were diluted in n-decane at a ratio of 1:10 for the feed and 1:1 for the treated oils, with 1000 ppm of cyclohexanol as internal standard. Compound identification was performed using the NIST 2017 library, requiring a minimum match factor of 85/100, typically exceeding 95/100 for most compounds. The concentration of identified compounds was determined by calibration of the most representative molecules using the internal standard method according to analogous procedures reported by Pagano et al. [5] Absolute errors were calculated by repeating the measurements twice.

The hydrodehalogenation degree (D_{HDH}) and the chlorine balance (Cl%) were estimated by determining the Cl content in all the fractions generated and collected during the experiments: used catalyst, treated oil, chemical solution tramps (bubblers), and reaction gases. In the case of the used catalysts, they were first washed in a Soxhlet

extractor with 100 mL of THF. Then, the chlorine content of the washing solution (W_s), the washed catalyst (W_c), and the treated oils (T_o, collected hourly) were determined via ion chromatography (IC 930 Compact IC Flex, Metrohm), equipped with a Metrosep A Supp 7-150/4.0 column, Metrosep A Supp 5 Guard/4.0 pre-column, and Metrohm suppressor module MSM II. Prior to IC analysis, active oxidative decomposition (AOD) was carried out following the procedures outlined in EPA 5050 and EPA 9056 A European standards, using a calorimetric pump (IKA). To ensure accuracy, all samples were analyzed in duplicate, and error bars were used to account for the measurement errors. The ion chromatograph was calibrated using a multi-component standard (containing F^-, Cl^-, NO_2^-, NO_3^-, PO_4^{3-}, and SO_4^{2-} at 10 ppm for each anion) from Reagecon, enabling indirect detection of halogen content. The Cl content in the aqueous phase (A_p) from the bubblers was also analyzed directly by IC. On the other hand, the presence of halogenated compounds in the produced gases was examined using a GC coupled with an electron capture detector (Agilent 8860 GC/ECD equipped with a CP-SilicaPLOT column (30 m x 320 μm x 4 μm).

The D_{HDH} was calculated based on the capacity of each catalyst to remove chlorine from the feedstock. The chlorine concentration (ppm) in the initial oil (C_i) and the treated oil (C_f) was measured, and D_{HDH} was calculated using equation 1:

$$D_{HDH}\,(\%) = \left(\frac{C_i - C_f}{C_i}\right) \times 100 \qquad (1)$$

Chlorine balance (Cl%) was calculated referring to the amount of Cl (in mg) obtained in each reaction fraction (solid, liquid, and gas) to that contained per gram of feed, according to equation 2:

$$Cl\% = \left(1 - \frac{\sum_i mg\ Cl\ in\ solid + \sum_i mg\ Cl\ in\ liquid + \sum_i mg\ Cl\ in\ gas}{g\ Cl\ in\ feed}\right) \times 100 \qquad (2)$$

However, in this work, the Cl content of the gaseous fraction was practically negligible, leaving only the solid and liquid fractions as the main contributors of Cl, which are calculated by equations 3 and 4:

$$\sum_i mg\ Cl\ in\ solid = mg\ Cl\ in\ W_c + mg\ Cl\ in\ W_s \quad (3)$$

where W_c is the washed catalyst and W_s is the washing THF solution after Soxhlet extraction treatment.

$$\sum_i mg\ Cl\ in\ liquid = mg\ Cl\ in\ oil + mg\ Cl\ in\ Aqueous\ bubblers \quad (4)$$

Overall, the chlorine balance achieved a minimum closure of 94 wt.% in all experiments.

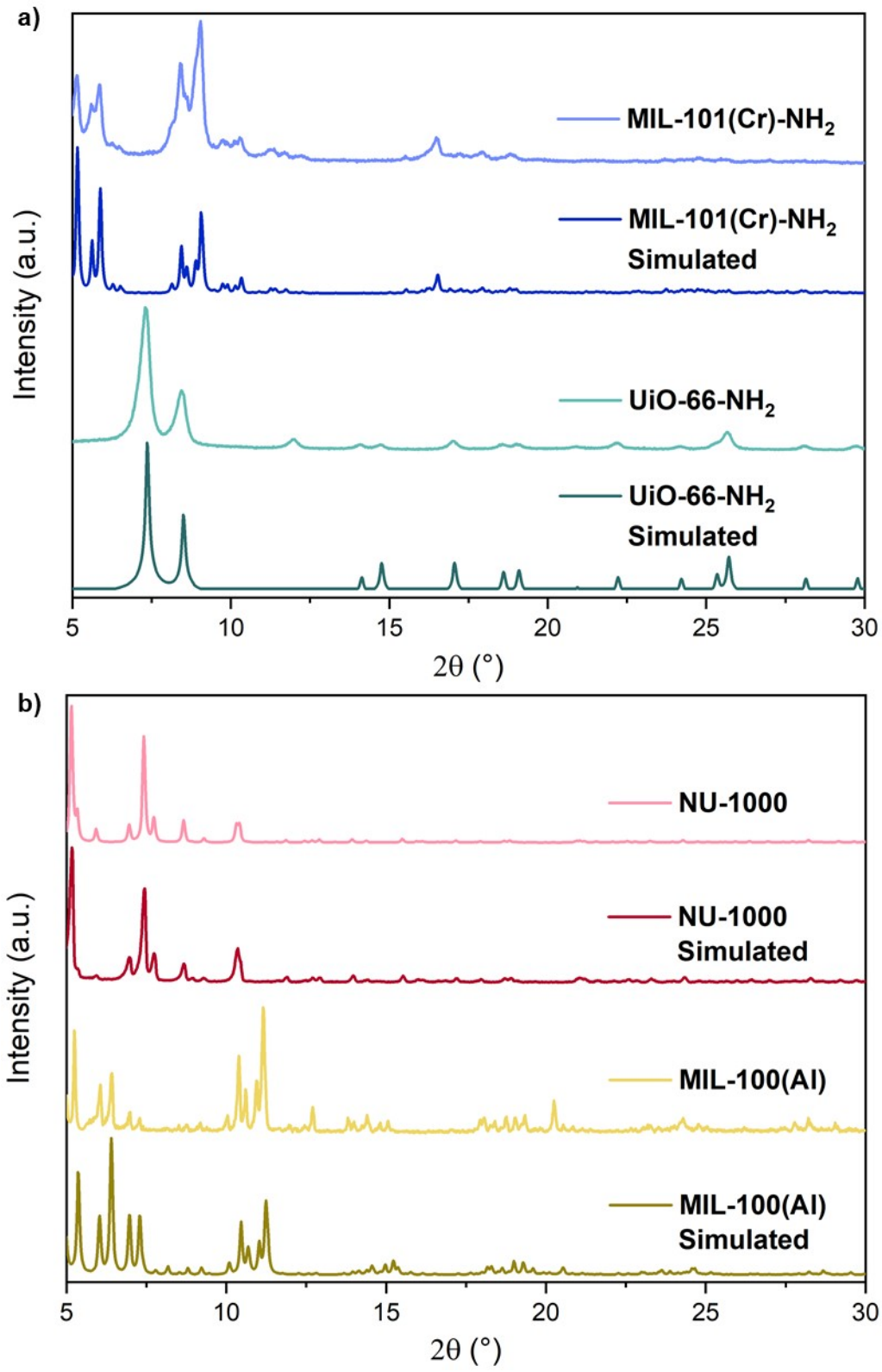

Fig. S1. Simulated PXRD patterns of all synthesized materials. a) Microwave MOFs, MIL-101(Cr)-NH_2 and UiO-66-NH_2, and b) Solvothermal MOFs, MIL-100(Al) and NU-1000.

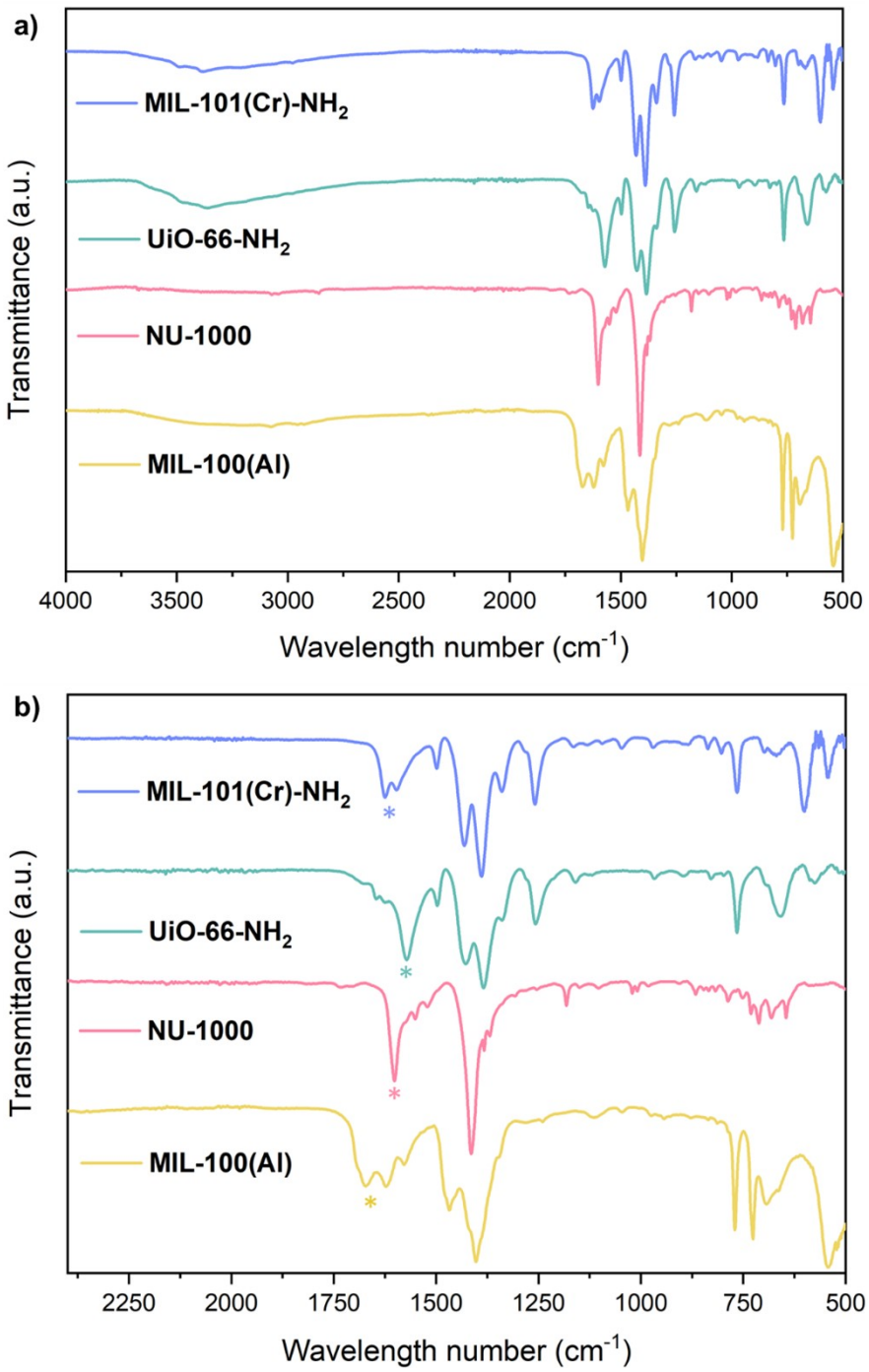

Fig. S2. a) ATR-FTIR spectra of MIL-101(Cr)-NH_2, UiO-66-NH_2, NU-1000 and MIL-100(Al). b) Correspond to their amplification within 500-2350 cm^{-1}. Asterisks indicate the bands assigned to the asymmetric stretching vibrations of coordinated carboxylate groups (ν_as(COO^-)), resulting from metal–ligand coordination and evidenced by characteristic shifts and intensity variations compared to the free linker.

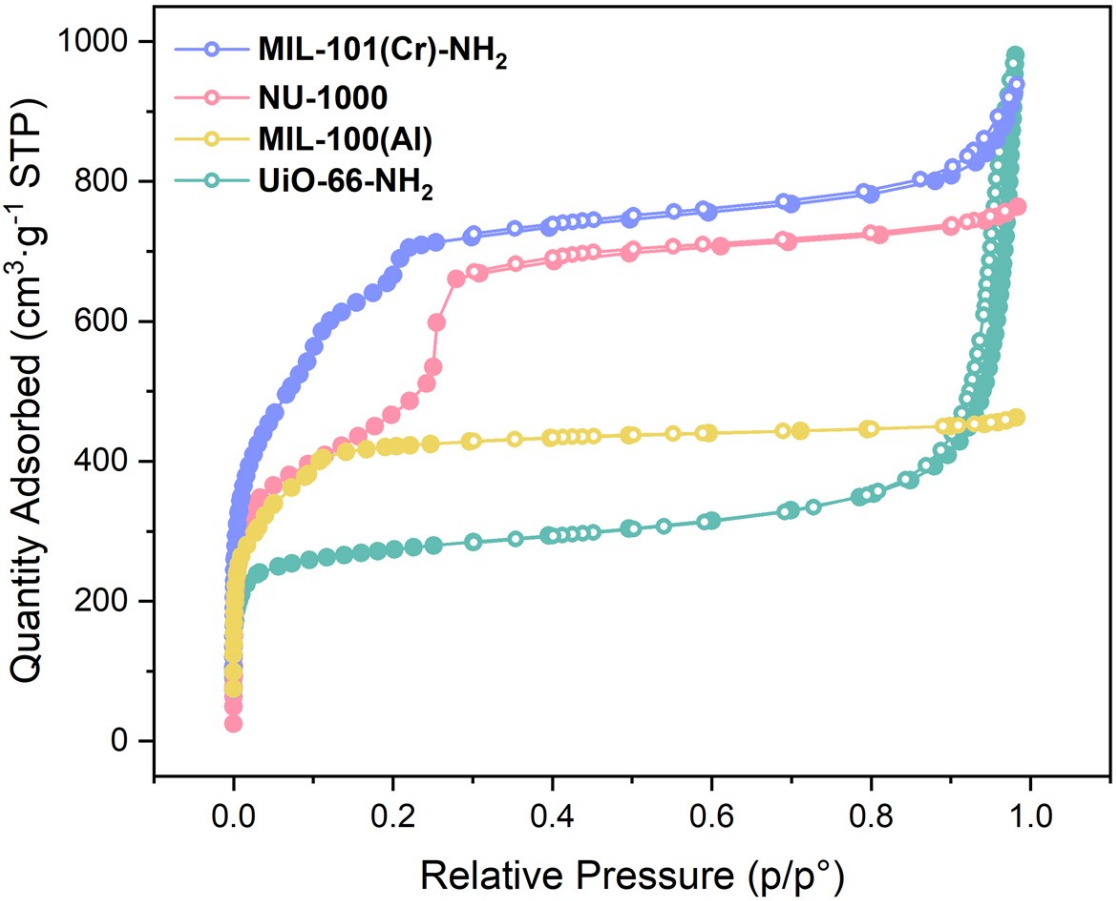

Fig. S3. Nitrogen sorption isotherms at 77 K of MIL-101(Cr)-NH_2, NU-1000, MIL-100(Al), and UiO-66-NH_2.

Table S1. Comparison of the textural properties of MIL-101(Cr)-NH_2, NU-1000, MIL-100(Al), and UiO-66-NH_2.

Properties	MIL-101(Cr)-NH_2	NU-1000	MIL-100(Al)	UiO-66-NH_2
S_{BET} ($m^2 \cdot g^{-1}$)	2344	1778	1539	1035
V_{PORE} ($cm^3 \cdot g^{-1}$)	1.24	1.49	0.62	0.34

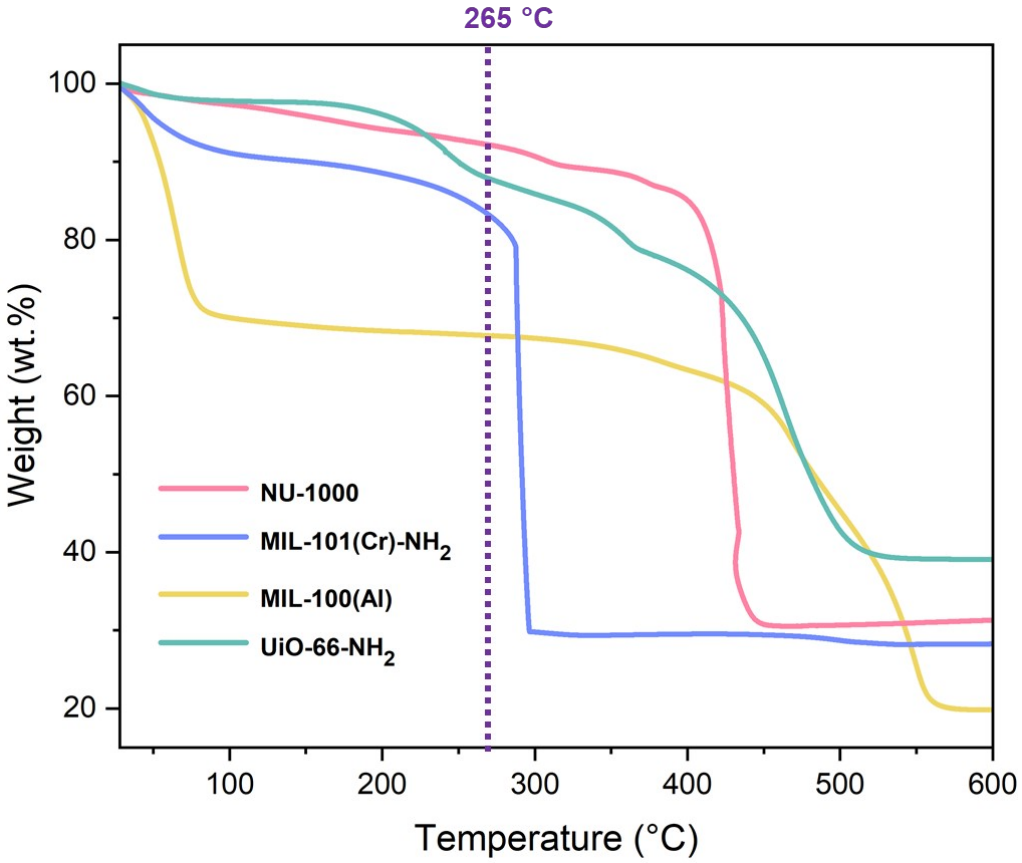

Fig. S4. TGA curves, in air, for different catalysts used in this work: NU-1000, MIL-101(Cr)-NH_2, MIL-100(Al) and UiO-66-NH_2. The purple dashed line indicates the temperature at which the HDH reaction is planned to occur.

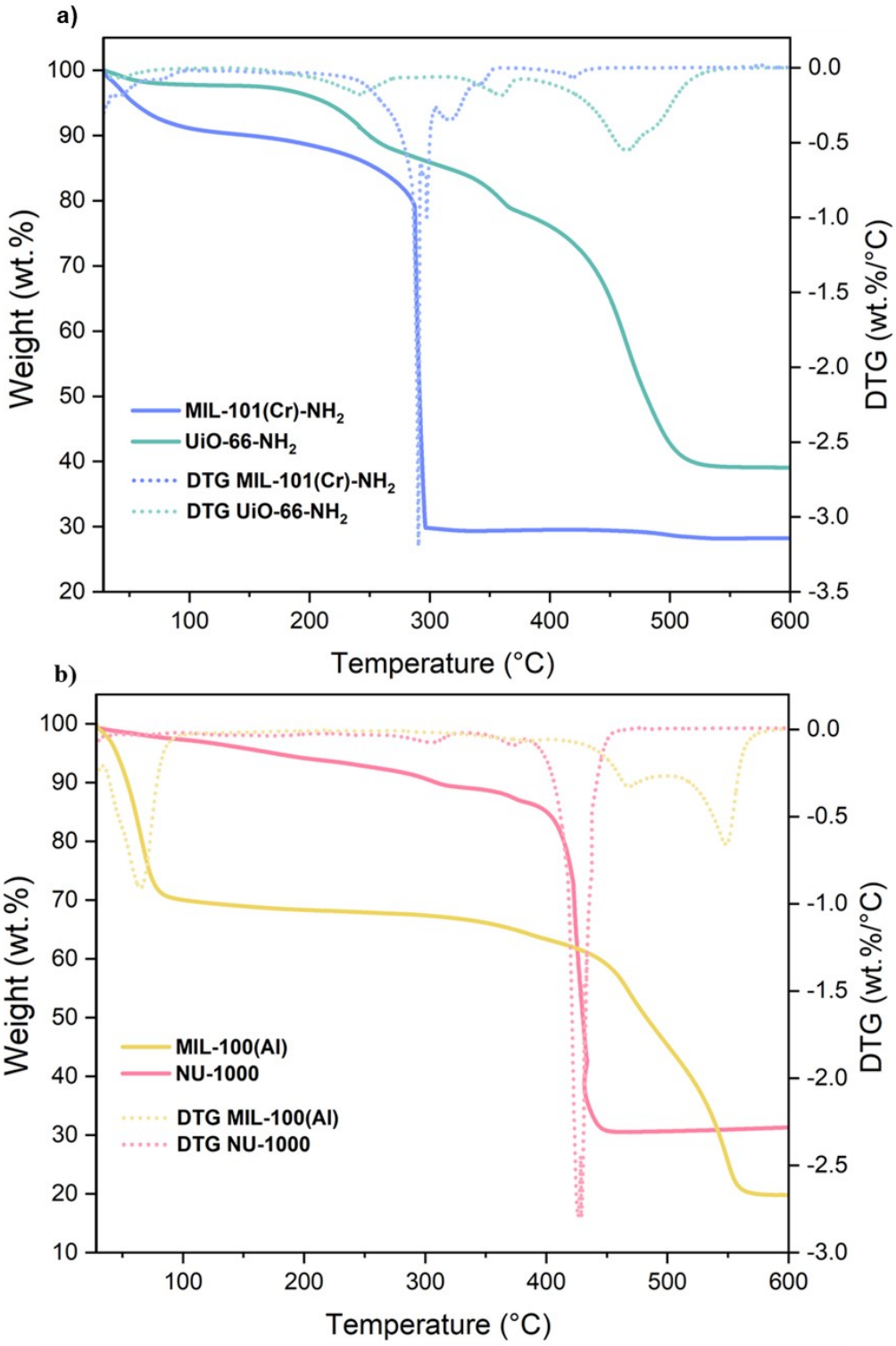

Fig. S5. TGA and DTG (Derivative Thermogravimetry) curves, under air, of a) Microwave MOFs, MIL-101(Cr)-NH_2 and UiO-66-NH_2, and b) Solvothermal MOFs, MIL-100(Al) and NU-1000.

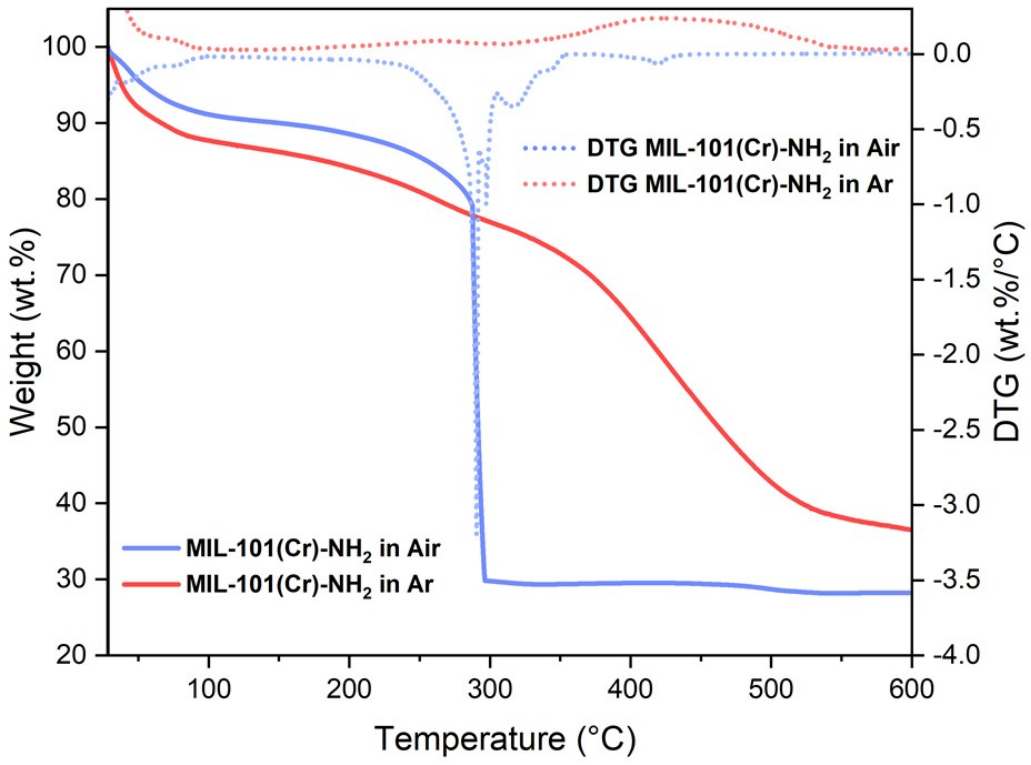

Fig. S6. TGA and DTG curves of MIL-101(Cr)-NH_2 (light blue) under air and MIL-101(Cr)-NH_2 (light red) under Ar.

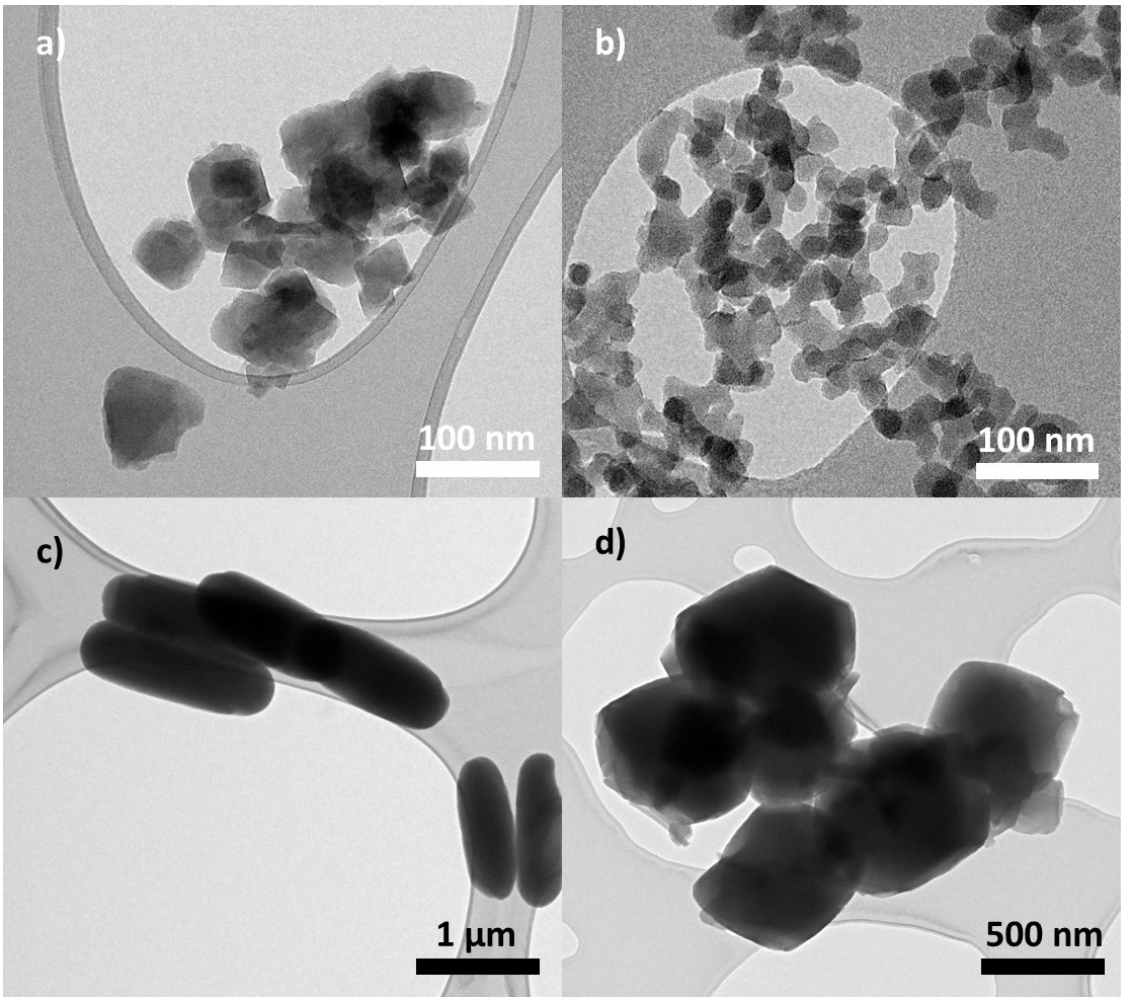

Fig. S7. TEM images of as-synthesized samples: a) MIL-101(Cr)-NH_2, b) UiO-66-NH_2, c) NU-1000 and d) MIL-100(Al).

Table S2. Comparison in the HDH activity of MIL-101(Cr)-NH_2 and UiO-66-NH_2 in 4 h.

MOF	Time (h)	Conversion (%)[a]	Selectivity (%)[a,b]	MOF	Time (h)	Conversion (%)	Selectivity (%)[a,b]
UiO-66-NH_2	1	100	79	**MIL-101(Cr)-NH_2**	1	97	84
	2	89	31		2	98	87
	3	69	29		3	100	25
	4	56	25		4	98	21

[a] Conversion and selectivity were determined by GC using cyclohexanol as internal standard and the corresponding products were identified by GC-MS.

[b] Selectivity to *n*-octane.

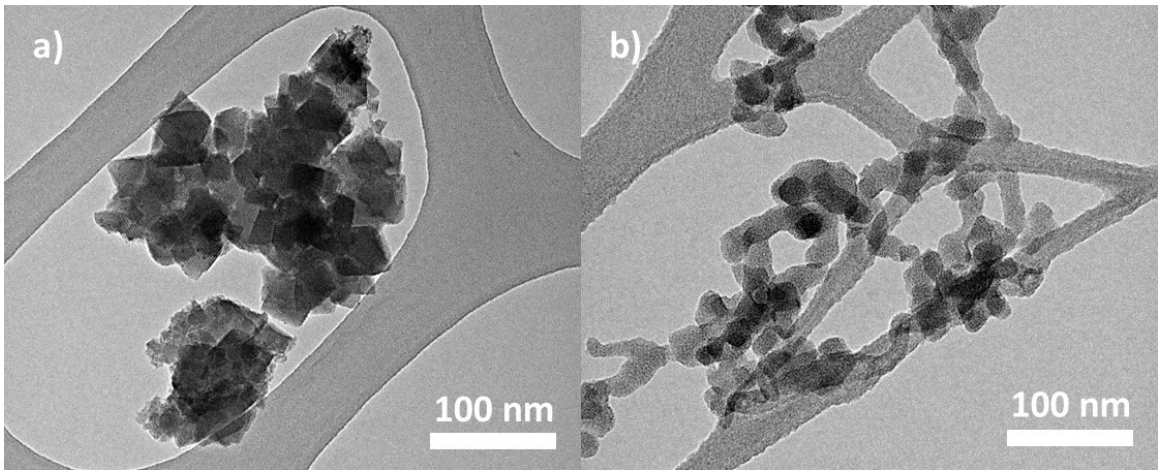

Fig. S8. TEM images of MOF samples after 4 h of HDH reaction: a) MIL-101(Cr)-NH_2-U and b) UiO-66-NH_2-U.

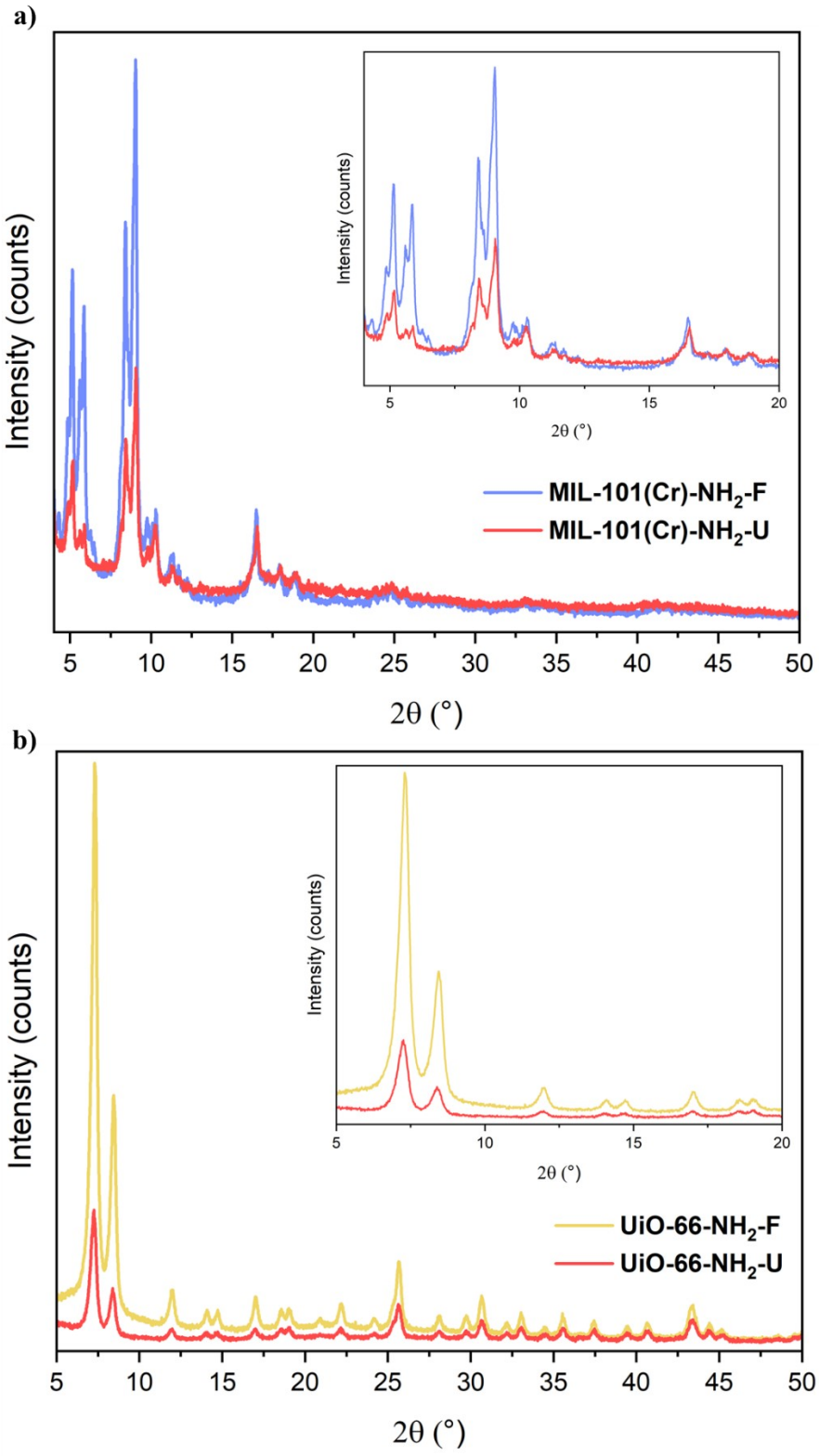

Fig. S9. PXRD patterns of a) MIL-101(Cr)-NH_2-F (fresh material, light blue) vs. MIL-101(Cr)-NH_2-U (material after 4 h-reaction, light red) and b) UiO-66-NH_2-F (fresh material, light yellow) vs. UiO-66-NH_2-U (material after 4 h-reaction, light red).

Table S3. Comparison of the properties of UiO-66-NH_2 and MIL-101(Cr)-NH_2.

Properties	**UiO-66-NH_2**	**MIL-101(Cr)-NH_2**
MOF Particle size (nm)	28±3	30±8
S_{BET} ($m^2 \cdot g^{-1}$)	1034	2344
V_{PORE} ($cm^3 \cdot g^{-1}$)	0.34	1.24
Lewis acid capacity	Zr^{4+}(stronger)	Cr^{3+}(weaker)
Presence of F^-	No	Yes
Defect	20% missing linkers	33% missing linkers

TGA Data Analysis for Defective MIL-101(Cr)-NH_2

To determine the number of defects in MIL-101(Cr)-NH_2, a similar study to that conducted by Yi Zhang *et al.* for MIL-101(Cr) [6] was carried out. First, the molecular weight used in our defect analysis was derived from the theoretical secondary building unit (SBU) of crystalline MIL-101(Cr)-NH_2, synthesized with KF as a modulator. This MOF is composed by $Cr_3(\mu_3\text{-}O)$ trimers connected to 2-aminoterephthalate linkers. In the KF-assisted synthesis, F^- serves as the charge-balancing ligand at the node. The molecular formula corresponding to the unit cell is:

$$[Cr_3(\mu_3\text{-}O)F(NH_2\text{-}BDC)_3(H_2O)_2] \rightarrow C_{24}H_{19}Cr_3FN_3O_{15}$$

Trough TGA and DRX, it was confirmed that the final residue after the complete combustion of MIL-101(Cr)-NH_2 is Cr_2O_3. The combustion reaction of the original MIL-101(Cr)-NH_2 can be represented as follows:

$$2C_{24}H_{19}Cr_3FN_3O_{15} + 45O_2 \longrightarrow 3Cr_2O_3 + 48CO_2 + 15H_2O + 2HF$$

The molecular weight of $C_{24}H_{19}Cr_3FN_3O_{15}$ is 764.40 $g{\cdot}mol^{-1}$, while the molecular weight of Cr_2O_3 is 151.99 $g{\cdot}mol^{-1}$. Based on these values, the theoretical weight loss of $H_2BDC\text{-}NH_2$ can be calculated as follows:

$$Theoretical\ weight\ loss = \frac{(764.4 - 151.99\ \times 1.5)}{764.4} \times 100\% = 70.17\%$$

From the TGA data, the observed weight loss of $H_2BDC\text{-}NH_2$ in MIL-101(Cr)-NH_2 decomposition (200 °C) is 47.17%. Using this value, the number of missing linkers can be determined with the following formula:

$$Number\ of\ missing\ linkers = 6\left(1 - \frac{47.17}{70.17}\right) = 1.96$$

This calculation indicates that the sample contains approximately 32.77% missing linkers.

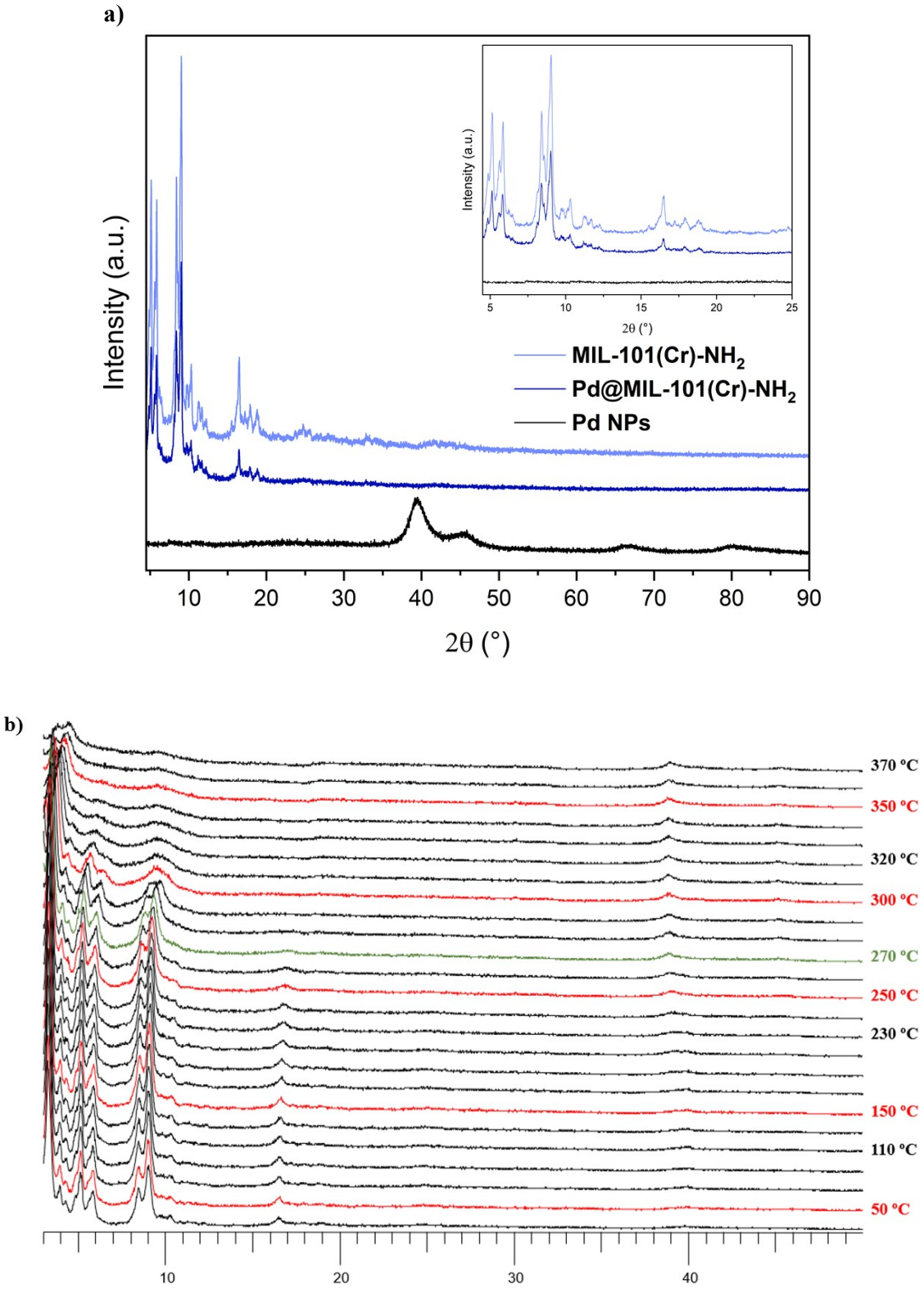

Fig. S10. a) PXRD patterns of MIL-101(Cr)-NH_2 (light blue), Pd(4.3%)@MIL-101(Cr)-NH_2 (dark blue) and Pd NPs (black) with a zoom from 5 to 25. b) Variable-temperature X-ray diffraction (VT-XRD) of Pd(4.3%)@MIL-101(Cr)-NH_2, indicating in green the temperature for HDH reaction.

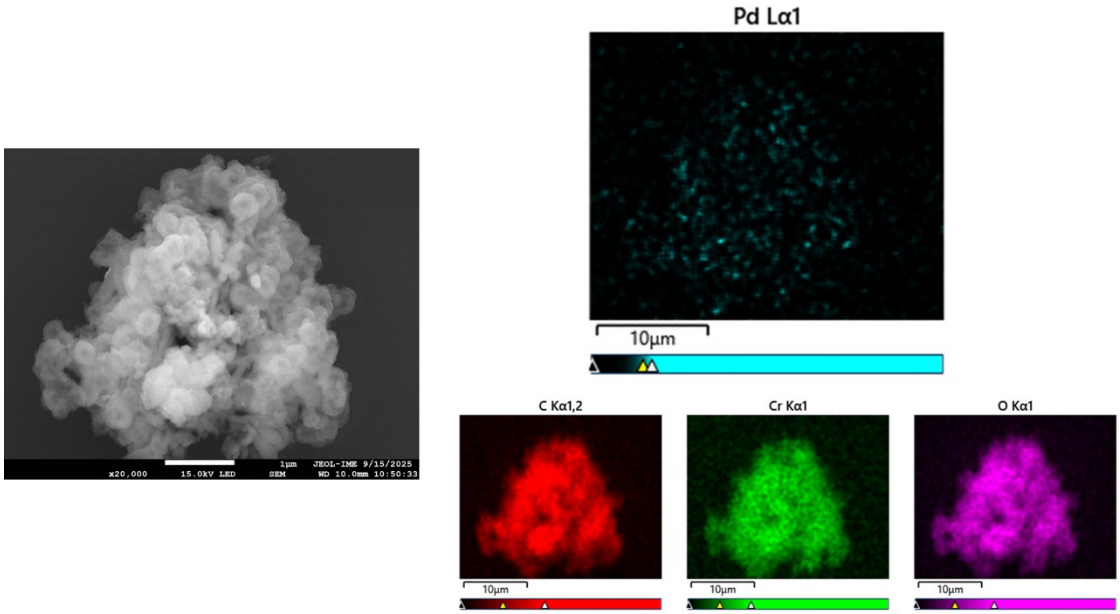

Fig. S11. FESEM images and elemental mapping of the Pd(4.3%)@MIL-101(Cr)-NH_2.

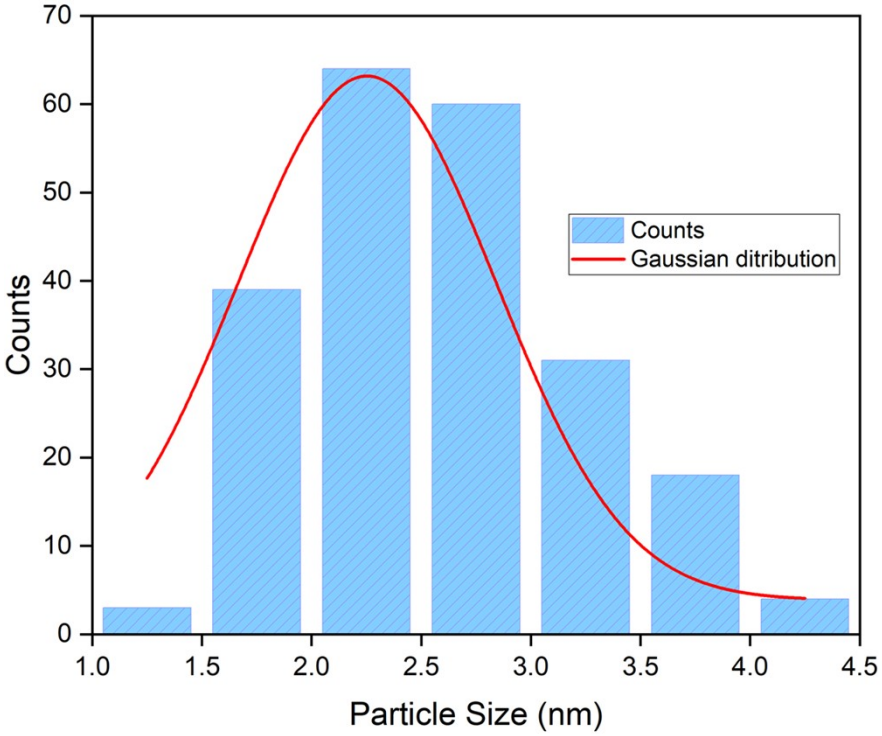

Fig. S12. Pd particle size distribution of Pd(4.3%)@MIL-101(Cr)-NH_2, (*n* = 220 Pd nanoparticles).

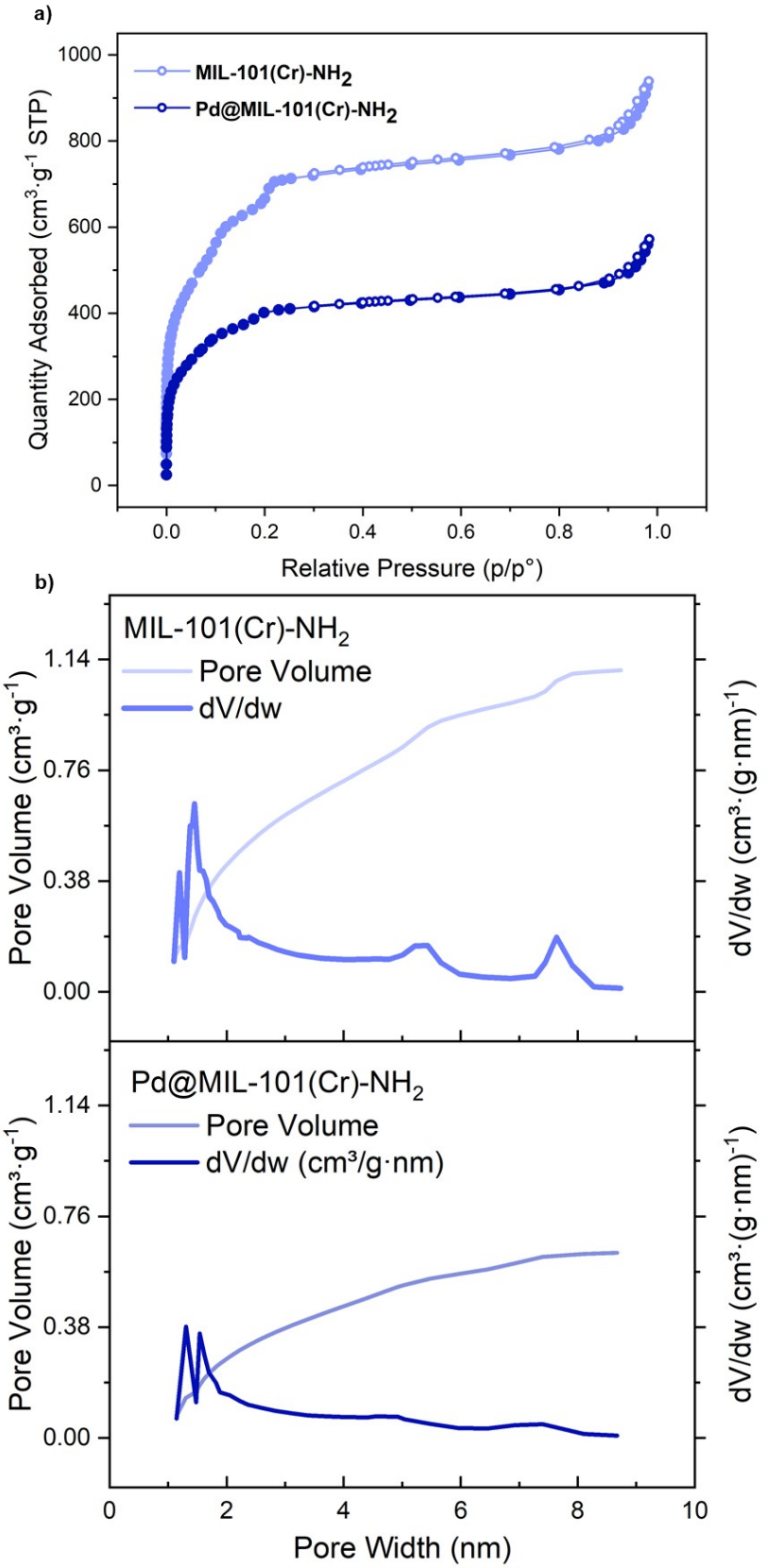

Fig. S13. a) Nitrogen sorption-desorption isotherms at 77K of MIL-101(Cr)-NH_2 (light blue) and Pd(4.3%)@MIL-101(Cr)-NH_2 (dark blue). b) Horvath-Kawazoe cumulative pore volume plot.

Table S4. Comparison of the textural properties of MIL-101(Cr)-NH_2 and Pd(4.3%)@MIL-101(Cr)-NH_2.

Properties	**MIL-101(Cr)-NH_2**	**Pd@MIL-101(Cr)-NH_2**
$\mathbf{S_{BET}}$ ($m^2 \cdot g^{-1}$)	2344	1391
$\mathbf{V_{PORE}}$ ($cm^3 \cdot g^{-1}$)	1.24	0.60

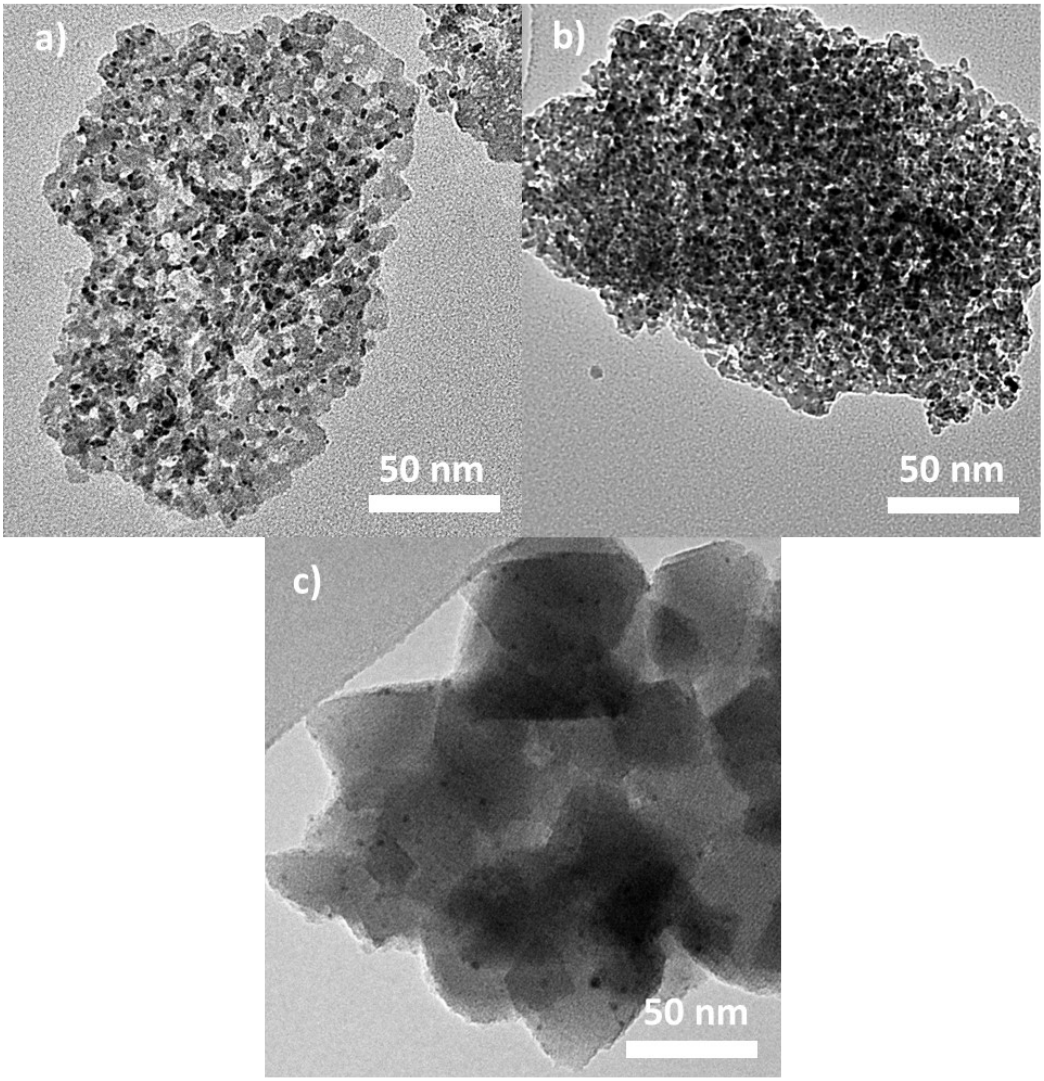

Fig. S14. TEM images of the commercial Pd(5%)/Al_2O_3 catalyst a) before reaction (fresh material), b) after 4 h of reaction (used material). c) TEM images of the composite Pd(4.3%)@MIL-101(Cr)-NH_2 after 4 h of reaction (used material).

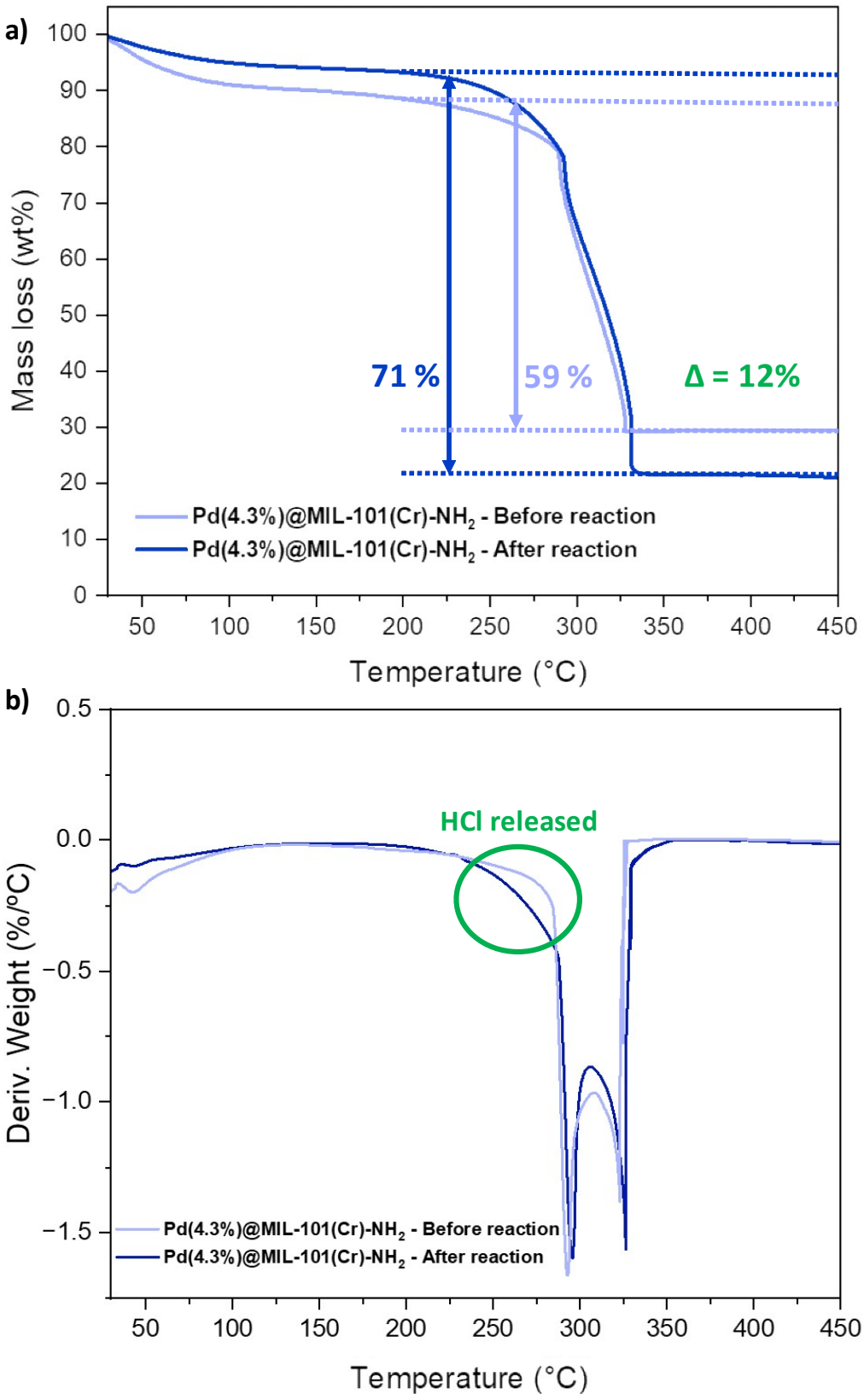

Fig. S15. a) TGA and b) DTG curves, in air, for Pd(4.3%)@MIL-101(Cr)-NH_2 before and after HDH reaction.

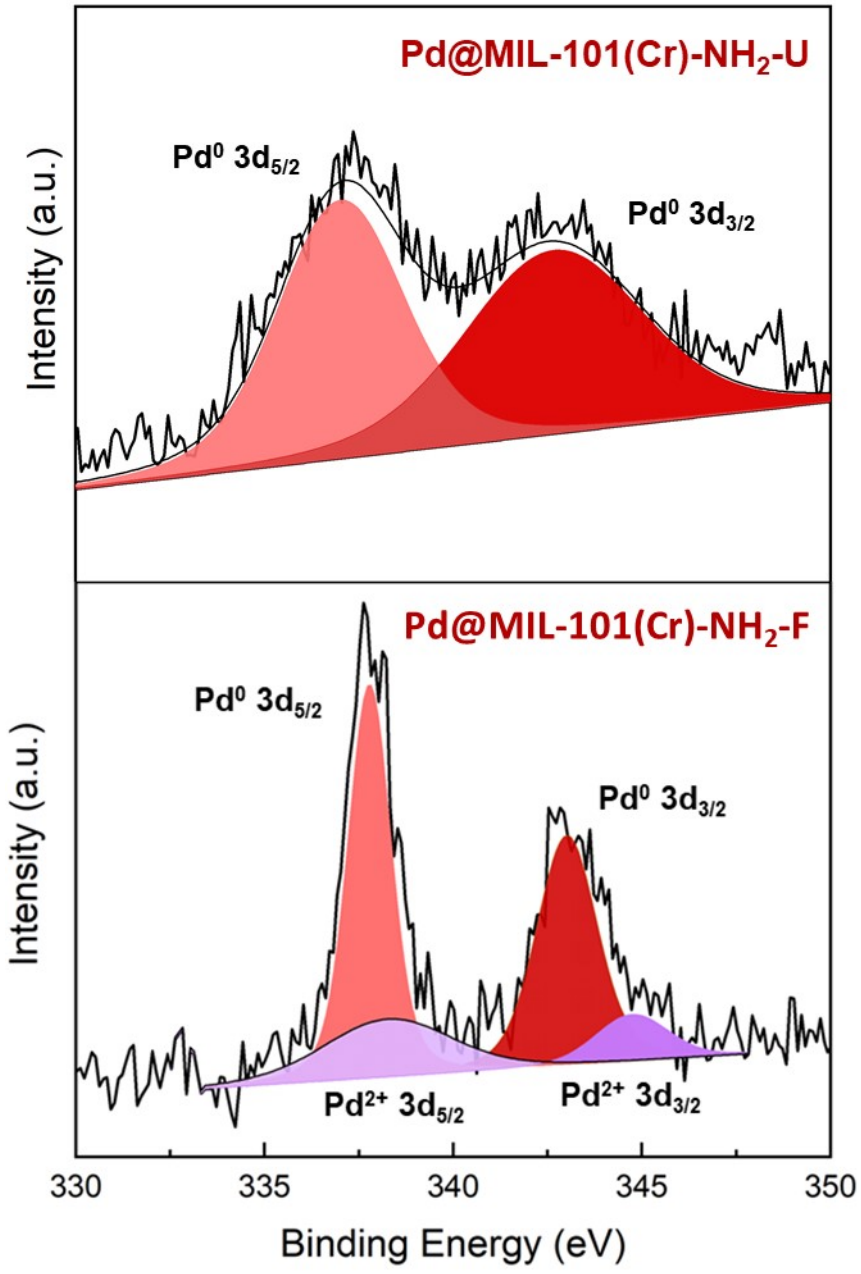

Fig. S16. XPS spectra of Pd 3d region for Pd@MIL-101(Cr)-NH_2-F (before reaction, fresh) and Pd@MIL-101(Cr)-NH_2-U (after 4 h of reaction, used).

Reference

1 C. Volkringer, D. Popov, T. Loiseau, G. Férey, M. Burghammer, C. Riekel, M. Haouas and F. Taulelle, *Chem. Mater.*, 2009, **21**, 5695–5697.

2 T. E. Webber, S. P. Desai, R. L. Combs, S. Bingham, C. C. Lu and R. L. Penn, *Cryst. Growth Des.*, 2020, **20**, 2965–2972.

3 R. M. Guerrero, I. D. Lemir, S. Carrasco, C. Fernández-Ruiz, S. Kavak, P. Pizarro, D. P. Serrano, S. Bals, P. Horcajada and Y. Pérez, *ACS Appl. Mater. Interfaces*, 2024, **16 (18)**, 24108−24121.

4 A. Carretero-Cerdán, S. Carrasco, A. Sanz-Marco, A. Jaworski and B. Martín-Matute, *Mater. Today Chem.*, 2023, **31**, 101618.

5 M. Pagano, H. Hernando, J. Cueto, P. L. Cruz, J. Dufour, I. Moreno and D. P. Serrano, *Chem. Eng. J.*, 2023, **454**, 140206.

6 Y. Zhang, C. Sun, Y. Ji, K. Bi, H. Tian and B. Wang, *Sep. Purif. Technol.*, 2024, **330**, 125293.